© February 2026 | IJIRT | Volume 12 Issue 9 | ISSN: 2349-6002

NMR And IR Spectroscopic Analysis of Anions of Enol Form of Isatin and Its Halogenated Derivatives: A Theoretical Study

Esha Arora
Department of Chemistry
Shyama Prasad Vidyalaya Lodi Estate, New Delhi-110003

***Abstract*—Anions of the enol (lactim) form of isatin and a series of halogenated derivatives were examined using density functional theory to understand how halogen substitution modulates electronic delocalization and, in turn, the vibrational and NMR spectroscopic response. Optimized structures, harmonic vibrational frequencies, and GIAO-based H-1 NMR and C-13 NMR chemical shifts were computed in a solvent environment representative of experimental conditions. The calculated IR spectra establish characteristic markers of conjugation and carbonyl non-equivalence in the anionic framework, while the NMR shielding trends identify substitution-sensitive ring positions and carbonyl centers that reflect charge redistribution within the π-system. The novelty of this work lies in presenting an integrated, correlation-based interpretation that links ground-state electronic delocalization mechanisms to both IR mode mixing and NMR shielding behavior for anionic lactim systems, which are comparatively less explored than neutral isatin derivatives. Overall, this study provides a unified theoretical framework for interpreting and predicting substituent-dependent spectroscopic signatures in isatin-based enolate anions, offering guidance for the rational design of functionalized heteroaromatic systems with tunable electronic properties.**

***Index Terms*—DFT; electron delocalization; enol (lactim) form; GIAO NMR; halogenated derivatives; IR spectroscopy; isatin anion; NBO analysis.**

I. INTRODUCTION

Isatin (1H-indole-2,3-dione) is a widely used heterocyclic scaffold in synthetic and medicinal chemistry, valued for its reactivity, modular functionalization, and ability to generate structurally diverse derivatives [1]. Beyond its neutral form, isatin can access multiple tautomeric and ionic states that often govern its chemical behavior under basic or catalytic conditions [1–3]. In particular, the enol (lactim) form and its anions are electronically activated species in which negative charge is redistributed across the carbonyl–nitrogen framework and the fused aromatic ring [2,3]. Such anionic lactim forms are important because they can influence site selectivity, nucleophilicity or electrophilicity balance, and reaction outcomes in condensation, substitution, and annulation pathways [1,3]. However, these species are frequently difficult to isolate experimentally, and their identification often relies on spectroscopic signatures and reliable theoretical interpretation [2–4]**.** Halogen substitution provides a practical strategy for tuning the electronic properties of aromatic heterocycles [1,2,18]. Halogens are routinely introduced during synthesis to modulate reactivity and stability, enable further derivatization through cross-coupling or substitution chemistry, and adjust physicochemical properties relevant to biological and materials applications **[**1,18]. In conjugated systems, halogens can exert strong inductive effects and, depending on the substitution pattern and polarizability, can also alter π-electron distribution through orbital interaction [18]. For isatin-based lactim anions, such substitution is expected to change how charge is delocalized across the ring–carbonyl network, thereby affecting the strength and coupling of key bonds [2,3,5–7]. Establishing predictable structure–spectra relationships for these substituted anions is therefore useful not only for fundamental understanding but also for guiding the design and characterization of functionalized isatin derivatives [2,3,5–7]**.** Among the most accessible and informative probes of electronic redistribution are infrared (IR) and nuclear magnetic resonance (NMR) spectra [4]. IR spectra are sensitive to bond strengths, charge localization, and dipole-derivative changes; hence, they are particularly effective for distinguishing carbonyl environments and diagnosing conjugation-controlled mode mixing in resonance-stabilized anions [2,3,4,17]. NMR chemical shifts, in turn, provide a site-resolved measure of magnetic shielding and therefore serve as a direct reporter of local electron density and substituent effects [4,11]. When interpreted together, IR and NMR can supply complementary evidence for tautomeric preference, carbonyl non-equivalence, and substitution-induced polarization, which are critical for assigning reactive ionic forms in solution and for understanding how substituents bias electron flow in the π-system [2–4,17]. Despite this practical importance, systematic IR–NMR interpretations for anionic lactim isatin derivatives remain comparatively limited, particularly in a way that explicitly connects spectral changes to quantified electronic delocalization mechanisms [2,3]**.** Density functional theory (DFT) offers an effective route to bridge this gap [8,9]. Harmonic frequency calculations enable detailed vibrational assignments and identification of diagnostic skeletal and carbonyl modes, while GIAO-based NMR calculations provide consistent prediction of ^1H-NMR and ^13C-NMR chemical shifts across related structures [9–11]. Importantly, Natural Bond Orbital (NBO) analysis supplies a chemically intuitive decomposition of stabilization into donor–acceptor interactions (e.g., lone-pair → π* and π → π* delocalization), allowing one to rationalize why specific bonds and atoms respond to substitution [15,16]. A correlation-based framework integrating these tools can therefore serve as a predictive guide: it can help assign experimental spectra, anticipate the impact of substituents, and identify the most electronically responsive sites that may control reactivity [2,3,5–7,15,16]. In this context, the present study provides a comparative theoretical investigation of the anions of the enol form of isatin and its halogenated derivatives, focusing on the utility-driven objective of developing spectroscopy-ready descriptors for substitution effects [2,3,5–7]. Using DFT-based vibrational analysis and GIAO-based NMR calculations in a solvent environment, we establish consistent spectral markers across the series and relate them to NBO-derived delocalization pathways [9–11,13–16]. The novelty and utility of this work lie in delivering an integrated interpretation that connects halogen-tuned electron delocalization to both IR mode mixing/carbonyl behavior and site-specific NMR shielding trends, thereby providing a practical theoretical reference for characterizing reactive isatin lactim anions and for guiding the design of substituted isatin systems with tailored electronic and spectroscopic properties**.** [2,3,5–7,15,16]

II. COMPUTATIONAL DETAILS

All quantum-chemical calculations were performed using Density Functional Theory (DFT) as implemented in the Gaussian 09 program package [19]. The geometries of the anionic enol (lactim) forms of isatin and its halogen-substituted derivatives were fully optimized at the B3LYP/6-311++G(d,p) level without imposing symmetry constraints [20,21,22,23]. The inclusion of diffuse and polarization functions in the 6-311++G(d,p) basis set is essential for an adequate description of anionic species and their delocalized electron density [22,23]. Harmonic vibrational frequency calculations were subsequently carried out at the same level of theory to confirm that each optimized structure corresponds to a true minimum on the potential energy surface (no imaginary frequencies), generate theoretical infrared (IR) spectra, and obtain normal-mode assignments **[24]**. To account for systematic anharmonicity and method-dependent deviations inherent to the harmonic approximation, the calculated vibrational wavenumbers were scaled using standard scaling factors (0.9613) recommended for the B3LYP/6-311++G(d,p) level [24,25]. H1-NMR and C13-NMR chemical shifts were computed using the gauge-independent atomic orbital (GIAO) method at the B3LYP/6-311++G(d,p) level [26]. The isotropic shielding constants were converted to chemical shifts on the δ scale by referencing to tetramethyl silane (TMS) calculated at the same level of theory [27]. These NMR computations were used to evaluate the impact of anionic character and halogen substitution on local shielding environments. For consistency with related theoretical studies and prior work, all calculations were performed in the gas phase.

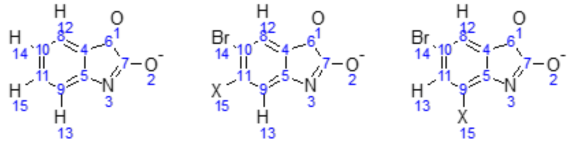

1a 1b 1c

Figure 1 Numbering scheme of enol form of anions of Isatin (1a), 10-Bromo-11-haloisatin (1b), 10-Bromo-9-haloisatin (1c) where X=F, Cl, Br

III. RESULTS AND DISCUSSION

3.1 NMR Spectra

The H-1 NMR and C-13 NMR chemical shifts of the isatin anion and its halogen-substituted derivatives (Figure 1) were computed using the gauge-independent atomic orbital (GIAO) method at the B3LYP/6-311++G(d,p) level with DMSO as solvent [28-31]. The isotropic shielding constants (σ) were converted to chemical shifts (δ, ppm) relative to tetramethyl silane (TMS) using:

$\delta_i = \sigma_{TMS} - \sigma_i$,

where σ_{TMS} (31.96 for H and 185.0 for C) were obtained at the same computational level. The calculated C-13 and H-1 chemical shifts together with natural charge densities are summarized in Table 1. Because magnetic shielding is sensitive to local electron density, the chemical shifts show a clear dependence on the natural atomic charges. To quantify this relationship, regression analysis was performed by correlating the calculated C-13 chemical shifts (y) with the corresponding natural charge densities (x) for each species. Polynomial fits and their coefficients of determination (R^2) are compiled in Table 2. Across the full set of eight species (ISTA, ISTA-10, ISTA-10A, ISTA-10B, ISTA-10C, ISTA-10D, ISTA-10E, and ISTA-10F), excellent correlations are obtained (R^2 = 0.9750–0.9999), indicating strong internal consistency between the charge distribution (NBO) and the computed NMR response [32,33].

3.1.1 NMR shift trends and interpretation

In all species, the most downfield C-13 resonances are associated with the carbonyl-bearing centers, reflecting strong deshielding in the anionic framework. The C6 site consistently appears at the highest chemical shift (≈207–210 ppm for most derivatives), followed by the C7 carbonyl carbon (≈180–182 ppm), while the C5 carbon also remains strongly deshielded (typically ≈171–187 ppm), consistent with its proximity to the heteroatom-containing segment and conjugated carbonyl system. The aromatic ring carbons C4 and C8 generally resonate in the expected aromatic region (≈125–137 ppm), whereas C9–C11 show substitution-sensitive behavior, with noticeable variations in both computed charge and δ values across the halogenated series. The computed H-1 shifts for the aromatic hydrogens fall in a narrow window (typically ~6.4–7.4 ppm), indicating that substitution perturbs the local electronic environment primarily through π-delocalization rather than large structural rearrangements. Where halogen substitution replaces an aromatic hydrogen (e.g., H14/H15 positions), the corresponding proton signal is absent, supporting the assigned substitution pattern. A strong correlation between calculated C-13 chemical shifts and NBO-derived natural charges is observed for each species (Table 2), with R^2 values ranging from 0.9750 to 0.9999. This confirms that changes in shielding are governed predominantly by charge redistribution within the conjugated framework: more positive (electron-deficient) carbon centers are generally more deshielded (higher δ), whereas electron-rich carbons show relative shielding (lower δ). The excellent correlations therefore provide internal consistency between the electronic structure (NBO charges) and the predicted NMR response, and support the substitution-dependent modulation of delocalization discussed in the vibrational section. In addition to the general trends, several positions show distinctly higher substitution sensitivity. Among the ring carbons, C9 displays the largest derivative-dependent variation, becoming markedly deshielded in ISTA-10D (δ(C9) = 160.9242 ppm) with a concomitant increase in positive natural charge (q = +0.37109), indicating substantial charge redistribution at this site. A second notable outlier is observed for C11 in ISTA-10A, where δ(C11) increases to 177.4687 ppm together with a large positive charge (q = +0.42881), consistent with a strongly electron-deficient environment at C11 relative to the remaining species. In contrast, the carbonyl centers remain consistently downfield across the series, with C6 typically appearing near ~208–210 ppm and C7 near ~180–182 ppm, supporting the persistence of two non-equivalent carbonyl environments within the anionic framework. The aromatic proton shifts fall within the expected region; however, H13 shows clear derivative-dependent deshielding, shifting from 6.3860 ppm (ISTA-10A) to 7.2436 ppm (ISTA-10E) and reaching 7.4488 ppm (ISTA-10F), in line with substitution-driven modulation of π-electron density around the corresponding ring position. Collectively, these site-specific changes (particularly at C9/C11 and H13) are consistent with the excellent charge–shift correlations (Table 2), reinforcing that local electronic redistribution within the conjugated backbone governs the computed NMR response. Across the halogen-substituted anionic enol series, the IR, NMR, UV–Vis, and NBO results are mutually consistent and collectively support substitution-dependent redistribution of electron density within a strongly conjugated framework. In the IR spectra, all derivatives exhibit an intense conjugation-driven skeletal band in the ~1600–1650 cm^{-1} region together with two distinct ν(C=O) bands (ν(C7=O2) and ν(C6=O1)), indicating non-equivalent carbonyl environments and strong vibrational coupling between the ring backbone and the heteroatom-containing segment. The NMR data reflect the same electronic asymmetry: C6 remains the most deshielded site (typically ~208–210 ppm) with C7 also consistently downfield (~180–182 ppm), while substitution-sensitive ring positions show larger δ changes where charge redistribution is strongest (e.g., C9 in ISTA-10D and C11 in ISTA-10A). These shift patterns track the NBO charge distribution and donor–acceptor delocalization pathways, where increased electron withdrawal (more positive natural charge) leads to decreased shielding (higher δ) and simultaneously enhances dipole-active vibrational intensity through stronger mode mixing. Consistent with this picture, the UV–Vis response (TD-DFT) captures enhanced π-delocalization through the dominant low-energy transitions, whose wavelengths and oscillator strengths are modulated by halogen substitution in the same directions as the IR intensity redistribution and NMR deshielding of electronically perturbed ring sites [7]. Overall, the convergence of IR mode mixing and carbonyl asymmetry, NMR charge-sensitive deshielding, TD-DFT $\pi \rightarrow \pi^*$/charge-transfer features, and NBO delocalization/charge trends provides a coherent spectroscopic validation of resonance stabilization in the anionic enol forms and its systematic tuning by halogen substitution [7].

Table 1 Calculated natural charge and chemical shifts (ppm) of carbons and hydrogens

	ISTA		ISTA-10		ISTA-10A		ISTA-10B	
Atom	Shift	Charge	Shift	Charge	Shift	Charge	Shift	Charge
C4	127.9455	-0.24221	128.6002	-0.22183	125.2018	-0.23240	127.2481	-0.22109
C5	186.32	0.21399	184.8964	0.21609	187.1755	0.23101	185.2421	0.22783
C6	209.7389	0.49089	209.3301	0.49396	206.2537	0.49161	185.225	0.49356
C7	181.3415	0.54931	181.0345	0.55228	181.5261	0.55714	180.9554	0.55481
C8	131.3647	-0.13953	134.3334	-0.16469	136.8986	-0.14295	135.9254	-0.14329
C9	122.9378	-0.26773	124.8699	-0.24513	110.4848	-0.30743	125.3225	-0.26709
C10	123.1581	-0.27232	132.8517	-0.15695	117.7095	-0.22480	130.8835	-0.19217
C11	147.6344	-0.15314	149.4954	-0.17862	177.4687	0.42881	159.9556	-0.02790
H12	7.2288	0.21378	7.2168	0.22926	7.2757	0.23249	7.271	0.23313
H13	6.6002	0.21289	6.561	0.21951	6.386	0.23473	6.7426	0.23175
H14/Br14	6.4947	0.21140	-	-	-	-	-	-
H15/X15	7.3402	0.20938	7.2118	-	-	-	-	-

	ISTA-10C		ISTA-10D		ISTA-10E		ISTA-10F	
Atom	Shift	Charge	Shift	Charge	Shift	Charge	Shift	Charge
C4	127.8556	-0.21942	130.5833	-0.20303	129.7261	-0.20058	129.3067	-0.19914
C5	184.2543	0.22736	171.6284	0.15602	180.6919	0.18707	182.3248	0.18325
C6	207.939	0.49398	207.7023	0.49498	208.287	0.49549	208.3464	0.49561

C7	181.1446	0.55435	180.1738	0.55398	180.404	0.55648	180.1816	0.55698
C8	135.6916	-0.14241	130.8715	-0.17572	133.1069	-0.16490	133.3844	-0.16332
C9	128.4672	-0.26917	160.9242	0.37109	135.6765	-0.07594	134.6978	-0.13963
C10	133.6442	-0.19658	131.2288	-0.14451	132.004	-0.14448	132.5734	-0.14425
C11	161.1599	-0.09271	135.2322	-0.24335	148.1883	-0.20271	151.3736	-0.20407
H12	7.2006	0.23323	7.1014	0.23298	7.1441	0.23334	7.0928	0.23356
H13	6.8128	0.23211	7.034	0.24148	7.2436	0.23891	7.4488	0.23891
H14/Br14	-	-	-	-	-	-	-	-
H15/X15	-	-	-	-	-	-	-	-

Table 2 Polynomial regression equations correlating C-13 chemical shift (y, ppm) with natural charge (x) for the anions of isatin and halogenated derivatives

S. No.	SPECIES	REGRESSION EQUATION (y vs x)	R²
1	ISTA	$y = 66348x^6 - 39651x^5 - 12998x^4 + 67095x^3 + 12913x^2 - 2153x - 214.7$	0.9997
2	ISTA-10	$y = 10^6x^6 - 83364x^5 - 21948x^4 + 13168x^3 + 22247x^2 - 4210x - 535.3$	0.9950
3	ISTA-10A	$y = -78167.2733x^6 + 43429.3131x^5 + 16966.442x^4 - 7991.4783x^3 - 1675.3496x^2 + 445.1533x + 207.3025$	0.9968
4	ISTA-10B	$y = -2262x^5 + 2390x^4 - 551.9x^3 - 284.7x^2 + 164.3x + 164.1$	0.9999
5	ISTA-10C	$y = -13466x^6 + 83262x^5 - 22702x^4 - 13713x^3 - 2063x^2 - 603.2x + 222.3$	0.9960
6	ISTA-10D	$y = -57542x^6 + 30888x^5 + 11138x^4 - 5144x^3 - 778.5x^2 + 238.1x + 164.3$	0.9990
7	ISTA-10E	$y = 34414x^6 - 28500x^5 + 3882x^4 + 27126x^3 + 902.6x^2 + 471.5x + 105.5$	0.9750
8	ISTA-10F	$y = 7 \times 10^6x^6 - 5 \times 10^6x^5 - 50766x^4 + 63633x^3 + 59281x^2 - 15109x - 1548$	0.9940

3.2 Vibrational Spectra

The calculated vibrational wavenumbers (cm⁻¹), IR intensities, and mode assignments for the isatin anion and its halogen-substituted derivatives are compiled in Tables 3–10. Harmonic frequency calculations were performed at the B3LYP/6-311++G(d,p) level for the anionic enol forms to obtain their infrared (IR) spectra and associated normal-mode compositions. The computed vibrational features provide molecular-level insight into bonding characteristics, carbonyl environments, and the extent of conjugation/charge delocalization across the heteroaromatic framework. In the discussion below, emphasis is placed on the most intense and structurally diagnostic modes—particularly the conjugation-driven skeletal stretching band in the ~1600–1650 cm⁻¹ region, the ν(C=O) stretching modes, and key mixed vibrations involving the C–N linkage and aromatic C–H deformations—so as to enable a consistent comparison across the substituted series. A selection of key vibrational modes with significant IR intensities is summarized and interpreted below.

3.2.1 ISTA

3.2.1.1 Dominant stretching bands and carbonyl region

The scaled IR spectrum of ISTA is characterized by a highly intense band at 1571.33 cm⁻¹ with intensity 684.07 a.u. (Table 3). This mode is a mixed skeletal stretching vibration dominated by ν(C4–C8) and ν(C9–C11) stretching, with additional contributions from symmetric stretching within the C11–C10–C8 fragment and motion involving the O2–C7 moiety, together with in-plane δ(C–H) components from C11–H15, C9–H13 and C8–H12. The high intensity and extensive mode mixing indicate efficient vibrational coupling across the conjugated framework of the anionic system. Two prominent absorptions appear in the carbonyl region at 1654.36 cm⁻¹ (I = 383.63 a.u.) and 1694.87 cm⁻¹ (I = 317.71 a.u.), assigned to ν(C7=O2) and ν(C6=O1), respectively. The presence of two distinct ν(C=O) bands reflects non-equivalent carbonyl environments governed by resonance interactions and charge redistribution in the enolate form.

3.2.1.2 Mid-frequency ring/resonance-coupled modes

In the mid-IR region, the band at 1273.77 cm⁻¹ (I = 229.37 a.u.) is assigned to antisymmetric stretching involving the C9–C5–N3 linkage together with contributions from the C11–C10–C8 segment, indicating coupling between the heteroatom-containing fragment and the aromatic skeleton. Additional ring-coupled modes at 1401.71 cm⁻¹ (I = 145.63 a.u.) and 1515.33 cm⁻¹ (I = 135.38 a.u.) arise from antisymmetric skeletal stretching coupled with in-plane δ(C–H) motions, which is typical for conjugated heterocyclic systems. A complex coupled vibration is observed at 1284.20 cm⁻¹ (I = 113.61 a.u.), featuring symmetric stretching of the C9–C5–N3 unit along with mixed skeletal stretching contributions from C4–C5–C9, C4–C5–N3, C11–C10–C8 and C10–C8–C4 fragments, coupled with in-plane δ(C–H) motions (H12, H13, H14, H15). The extensive mixed character of these modes supports strong vibrational communication across the molecular core.

3.2.1.3 N–C and aromatic C–H stretching

The bands at 1167.18 cm⁻¹ (I = 86.02 a.u.) and 1094.37 cm⁻¹ (I = 118.03 a.u.) are assigned to ν(N3–C7) and ν(C9–C11), respectively, each coupled with in-plane δ(C–H) contributions. The high-frequency band at 3039.90 cm⁻¹ (I = 60.14 a.u.) is attributed to aromatic/olefinic ν(C–H) stretching involving C8–H12, C9–H13 and C10–H14, appearing in the expected region for sp² C–H stretching vibrations.

3.2.1.4 Out-of-plane deformations

A characteristic deformation band at 692.03 cm⁻¹ (I = 49.83 a.u.) is assigned to out-of-plane γ(C–H) bending involving C8–H12, C9–H13, C10–H14 and C11–H15. Such modes are sensitive to ring planarity and substitution effects and therefore provide useful comparative markers across the derivative series.

3.2.1.5 Overall spectral features and implications

Overall, the IR spectrum of ISTA is dominated by intense conjugation-driven mixed skeletal stretching, two strong ν(C=O) bands reflecting distinct carbonyl environments, and ring deformation modes coupled with in-plane and out-of-plane C–H bending. The pronounced mode coupling and intensity distribution are consistent with a delocalized electronic structure and align with resonance features inferred from NBO analysis. [7] Any discussion of lactam–lactim tautomeric contributions should be framed comparatively across the full series using systematic trends in ν(C=O) and ν(C–N), and expressed cautiously as being consistent with spectroscopic behavior rather than definitive from IR data alone.

Table 3 Vibrational Spectra of ISTA

S.NO	FREQ	SCALED FREQ	INTENSITY	DESCRIPTION
1	1634.60	1571.33	684.0691	Stretching mode of C4-C8 bond and C9-C11 bond coupled with symmetric stretching of C11-C10-C8 and O2-C7 along with bending mode of C11-H15, C9-H13 and C8-H12
2	1720.96	1654.36	383.6311	Stretching mode of C7-O2
3	1763.10	1694.87	317.7077	Stretching mode of C6-O1
4	1325.05	1273.77	229.3659	Antisymmetric stretch of C9-C5-N3, C11-C10-C8, C10-C8-C4 and C8-C4-C5 bonds
5	1458.13	1401.71	145.6292	Antisymmetric stretch of C4-C5-N3 coupled with in plane bending mode of C8-H12 and C9-H13
6	1576.32	1515.33	135.3767	Antisymmetric stretch of C11-C10-C8 and C4-C5-C9 coupled with in plane bending of C10-H14, C11-H15 and C9-H13 bonds
7	1138.43	1094.37	118.0311	Stretching mode of C9-C11 coupled with in plane bending of H15-C11 and H13-C9 bonds

8	1335.90	1284.20	113.6063	Symmetric stretching mode of C9-C5-N3 coupled with antisymmetric stretch of C4-C5-C9, C4-C5-N3, C11-C10-C8, C10-C8-C4 and bending mode of H12-C8, H14-C10, H15-C11, H13-C9
9	1497.71	1439.78	95.8549	Stretching mode of C9-C11 coupled with in plane bending mode of C10-H14 and C11-H15
10	1214.17	1167.18	86.0205	Stretching mode of N3-C7 coupled with in plane bending mode of C8-H12 and C9-H13
11	3162.29	3039.90	60.1392	Stretching mode of C8-H12, C9-H13, C10-H14
12	719.89	692.03	49.8297	Out of plane bending of C8-H12, C10-H14, C11-H15, C9-H13

3.2.2 ISTA10

3.2.2.1 High-intensity carbonyl and ring-coupled vibrations

The scaled IR spectrum of ISTA10 (Table 4) displays prominent mixed skeletal modes in the ~1500–1701 cm^{-1} region (Table 4), together with strong C–N/C–C coupled vibrations in the ~1220–1410 cm^{-1} region. Overall, the band pattern is consistent with a resonance-stabilized anionic enol framework in which the carbonyl groups, the N3-containing linkage and the aromatic skeleton contribute cooperatively to dipole-active vibrations. The most intense feature is observed at 1557.65 cm^{-1} (I = 562.21 a.u.) and is assigned to a highly mixed stretching mode involving ν(C4–C8), ν(C9–C11) and ν(C5–N3), with contributions from the O2–C7 moiety, coupled with in-plane δ(C–H) components from C8–H12, C11–H14 and C9–H13. The large intensity and extensive mode mixing indicate efficient vibrational coupling across the conjugated framework. A strong carbonyl-associated band occurs at 1660.36 cm^{-1} (I = 506.26 a.u.) and is attributed mainly to ν(C7=O2), with minor coupling from the adjacent ring fragment (C9–C5), suggesting vibrational communication between the carbonyl group and the aromatic skeleton. The second carbonyl stretching band appears at 1701.29 cm^{-1} (I = 309.44 a.u.) and is assigned to ν(C6=O1), supporting a distinct carbonyl environment at C6 under the anionic electronic distribution.

3.2.2.2 Backbone and side-chain vibrational coupling

A pronounced band at 1269.70 cm^{-1} (I = 362.78 a.u.) is dominated by ν(C5–N3) coupled with in-plane δ(C–H) bending of C11–H14, C8–H12 and C9–H13. This assignment highlights the participation of the C5–N3 linkage as a key structural element in the mid-frequency region, consistent with its role in conjugation and charge delocalization. The mode at 1407.78 cm^{-1} (I = 308.68 a.u.) involves symmetric stretching centered on the C10–C8–C4 framework, with additional contributions from ν(C5–N3) and ν(C11–C9), accompanied by in-plane δ(C–H) motion (notably C11–H14). The mixed nature of this vibration indicates mechanical coupling between the ring backbone and the heteroatom-containing segment. At 1504.41 cm^{-1} (I = 129.35 a.u.), an antisymmetric skeletal stretching vibration is obtained, primarily involving the C4–C5–C9 fragment together with contributions from C4–C5, C10–C11 and the O2–C7 moiety, coupled with δ(C–H) bending of C11–H14 and C9–H13. Such composite modes are characteristic of conjugated systems where skeletal stretching couples with carbonyl-adjacent bond motion.

3.2.2.3 Mid-IR bending and mixed stretching modes

In the lower mid-IR region, the bands at 1162.19 cm^{-1} (I = 75.00 a.u.) and 1096.43 cm^{-1} (I = 76.38 a.u.) arise from vibrations involving the N3–C7 linkage and in-plane δ(C–H) scissoring/rocking components of aromatic hydrogens (notably C8–H12 and C9–H13/C11–H14). These features emphasize coupling between the heteroatom bridge and the aromatic periphery. The band at 1387.57 cm^{-1} (I = 69.55 a.u.) is assigned to an in-plane scissoring-type deformation involving the C9–C5–N3 fragment along with δ(C–H) contributions from C8–H12 and C9–H13. A composite mode at 1249.00 cm^{-1} (I = 69.13 a.u.) combines antisymmetric stretching of C11–C10–C8, C11–C9–C5 and C8–C4–C5 with symmetric stretching of C9–C5–N3, coupled to δ(C–H) bending (C11–H14 and C9–H13), reflecting distributed backbone flexibility within the conjugated network. The lower-intensity feature at 1220.93 cm^{-1} (I = 47.60 a.u.) corresponds mainly to in-plane rocking of C8–H12, C9–H13 and C11–H14.

3.2.2.4 Overall spectral features and implications

The scaled IR profile of ISTA10 is dominated by an intense mixed skeletal stretching band at 1557.65 cm⁻¹, two strong carbonyl stretching features at 1660.36 cm⁻¹ and 1701.29 cm⁻¹ corresponding to non-equivalent C=O environments, and prominent mid-frequency modes involving the C5–N3 and N3–C7 linkages coupled with aromatic C–H deformations. Collectively, these assignments are consistent with strong vibrational coupling across the molecular framework. The observed intensity distribution and mode mixing provide vibrational support for the electronic delocalization trends in the NBO and UV–Vis sections [7], while any tautomeric inference should be presented comparatively across the full series using systematic trends in ν(C=O) and ν(C–N) bands.

Table 4 Vibrational Spectra of ISTA10

S.NO	FREQ	SCALED FREQ	INTENSITY	DESCRIPTION
1	1620.36	1557.65	562.2141	Stretching mode of C4-C8, C9-C11, C5-N3, C7-O2 coupled with in plane bending mode of C8-H12, C11-H14 and C9-H13
2	1727.20	1660.36	506.2563	Stretching vibration of C7-O2 coupled with slight stretching vibration of C9-C5 bond
3	1320.82	1269.70	362.7830	Stretching vibration of C5-N3 bond coupled with in plane bending of C11-H14, C8-H12 and C9-H13 bond
4	1769.78	1701.29	309.4387	Stretching vibration of C6-O1 bond
5	1464.44	1407.78	308.6838	Symmetric stretching vibration of C10-C8-C4 coupled with stretching vibration of C5-N3, C11-C9 and in plane bending of C11-H14
6	1564.96	1504.41	129.3526	Antisymmetric stretching vibration of C4-C5-C9 bond coupled with stretching vibration of C4-C5, C10-C11, C7-O2 and bending mode of C11-H14, C9-H13 bonds
7	1140.57	1096.43	76.3793	In plane bending (scizzoring) of C11-H14 and C9-H13 bonds
8	1208.99	1162.19	75.0045	Stretching mode of N3-C7 coupled with coupled with bending mode of C8-H12 and C9-H13
9	1443.43	1387.57	69.5472	In plane bending mode of C9-C5-N3 (scizzoring), C8-H12, and C9-H13
10	1299.27	1249.00	69.1338	Antisymmetric stretching of C11-C10-C8, C11-C9-C5, C8-C4-C5 coupled with symmetric stretching of C9-C5-N3 and bending mode of C11-H14, C9-H13 bonds
11	1270.07	1220.93	47.6041	In plane bending of C8-H12 and C11-H14, C9-H13 (rocking)

3.2.3 ISTA-10A

3.2.3.1 High-intensity carbonyl and π-system modes

The scaled IR spectrum of ISTA-10A (Table 5) is dominated by intense conjugation-driven skeletal stretching features in the ~1568–1703 cm⁻¹ region, together with characteristic ring/bridge vibrations involving the C4–C5–N3 and N3–C7 linkages. The overall band pattern is consistent with strong vibrational coupling within the anionic enol framework, where substituent-induced changes in charge distribution contribute to mode mixing and intensity through enhanced dipole-moment variation. The most intense band appears at 1568.03 cm⁻¹ (I = 720.93 a.u.) and is assigned primarily to a mixed skeletal stretching mode dominated by ν(C9–C11) and ν(C4–C8), i.e., stretching along the extended conjugated pathway. The exceptionally high intensity and mixed character indicate efficient coupling across the conjugated backbone in the anionic form. Two prominent carbonyl-associated bands are observed at 1667.98 cm⁻¹ (I = 435.30 a.u.) and 1702.61 cm⁻¹ (I = 300.30 a.u.). The 1667.98 cm⁻¹ vibration is attributed mainly to ν(C7=O2) with minor coupling from adjacent ring motion (C9–C5), indicating measurable vibrational communication between the carbonyl site and the aromatic framework. In contrast, the 1702.61 cm⁻¹ band corresponds to ν(C6=O1) and appears comparatively more localized, suggesting weaker coupling of this carbonyl group with the conjugated manifold under the present electronic distribution.

3.2.3.2 Conjugated ring and bridge-linkage vibrations

A strong band at 1385.54 cm⁻¹ (I = 380.13 a.u.) is assigned to antisymmetric stretching involving the C4–C5–N3 fragment, coupled with in-plane δ(C–H) motions of C8–H12 and C9–H13. This mixed character indicates that the C4–C5–N3 unit participates actively in the conjugated vibrational manifold and couples effectively to peripheral aromatic C–H deformations. The mode at 1503.23 cm⁻¹ (I = 357.42 a.u.) corresponds to antisymmetric skeletal stretching involving the C11–C10–C8 and C4–C5–C9 fragments, coupled with δ(C9–H13). Such collective ring stretching modes are characteristic of conjugated systems and indicate strong mechanical coupling across the two ring segments. The band at 1279.56 cm⁻¹ (I = 203.55 a.u.) is assigned to stretching contributions from C10–C11 together with N3–C5, reflecting the vibrational participation of the bridge region connecting the heteroatom center to the aromatic skeleton.

3.2.3.3 C–H bending coupled to the N3–C7 linkage

Bands at 1188.57 cm⁻¹ (I = 195.82 a.u.) and 1163.41 cm⁻¹ (I = 190.68 a.u.) are dominated by in-plane δ(C–H) bending of C8–H12 and C9–H13, with minor contributions from ν(N3–C7). The repeated appearance of coupled δ(C–H)/ν(N3–C7) character suggests that these deformations remain dynamically connected to the conjugated framework rather than behaving as purely localized oscillations in the anionic structure.

3.2.3.4 Lower-frequency coupled stretching

A weaker feature at 1077.40 cm⁻¹ (I = 45.97 a.u.) is assigned to ν(C4–C6) coupled with δ(C9–H13). Although lower in intensity, it reflects secondary coupling pathways within the core skeleton and complements the higher-frequency conjugation-dominated modes.

3.2.3.5 Overall spectral features and implications

ISTA-10A exhibits a very intense conjugation-driven skeletal stretching band at 1568.03 cm⁻¹, two carbonyl stretching bands at 1667.98 cm⁻¹ and 1702.61 cm⁻¹ indicating non-equivalent C=O environments, and strong mixed modes involving the C4–C5–N3 and N3–C7 linkages coupled with aromatic δ(C–H) deformations. Overall, the assignments suggest that the ν(C7=O2) mode shows slightly stronger coupling with the π-network than ν(C6=O1), while the bridge region (C4–C5–N3 / N3–C7) acts as an effective conduit for vibrational communication across the molecular framework. These trends are consistent with the delocalization patterns inferred from NBO analysis and with conjugation effects reflected in the UV–Vis transitions [7].

Table 5 Vibrational Spectra of ISTA10A

S.NO	FREQ	SCALED FREQ	INTENSITY	DESCRIPTION
1	1631.17	1568.03	720.9338	Stretching vibration of C9-C11 and C4-C8 bonds
2	1734.09	1667.98	435.3048	Stretching vibration of O2-C7 bond coupled with slight stretching vibration of C9-C5 bond
3	1441.32	1385.54	380.1280	Antisymmetric stretch of C4-C5-N3 coupled with bending mode of C8-H12 and C9-H13 bonds
4	1563.74	1503.23	357.4184	Antisymmetric stretch of C11-C10-C8 and C4-C5-C9 coupled with bending mode of C9-H13 bond
5	1771.15	1702.61	300.2972	Stretching vibration mode of C6-O1 bond
6	1331.07	1279.56	203.5515	Stretching vibration of C10-C11 and N3-C5 bond
7	1236.42	1188.57	195.8184	Bending mode of C8-H12 and C9-H13 bond coupled with slight stretching mode of N3-C7 bond

8	1210.26	1163.41	190.6785	Bending mode of C8-H12 bond coupled with stretching mode of N3-C7 bond
9	1120.76	1077.40	45.9728	Stretching mode of C4-C6 coupled with bending mode of C9-H13 bond

3.2.4 ISTA-10B

3.2.4.1 High-intensity carbonyl and ring-conjugated vibrations

The scaled IR spectrum of ISTA-10B (Table 6) is dominated by intense conjugation-driven skeletal stretching in the ~1558–1705 cm⁻¹ region, accompanied by strong mid-frequency backbone modes and characteristic in-plane deformation bands. The distribution of intensities and the extent of mode mixing indicate efficient vibrational coupling across the aromatic framework and the N3-bridged segment in the anionic enol form. The most intense absorption is located at 1558.29 cm⁻¹ (I = 764.61 a.u.) and corresponds to a strongly mixed skeletal mode comprising antisymmetric stretching contributions from the C11–C9–C5 and C9–C5–N3 fragments, coupled with ν(C4–C8) and in-plane δ(C8–H12). The high intensity and extensive coupling indicate strong participation of the conjugated network in this dipole-active vibration. Two prominent carbonyl bands are observed at 1665.87 cm⁻¹ (I = 475.94 a.u.) and 1705.15 cm⁻¹ (I = 312.47 a.u.), assigned to ν(C7=O2) and ν(C6=O1), respectively. The persistence of two distinct ν(C=O) features indicates non-equivalent carbonyl environments under the anionic electronic distribution. The ν(C7=O2) band appears more strongly integrated with the conjugated manifold, whereas ν(C6=O1) is comparatively more localized.

3.2.4.2 Delocalized π-system and backbone stretching modes

A strong skeletal band at 1484.73 cm⁻¹ (I = 258.56 a.u.) is assigned to antisymmetric stretching of the C4–C5–C9 and C11–C10–C8 fragments, reflecting cooperative motion across both sides of the aromatic skeleton. The mode at 1367.95 cm⁻¹ (I = 215.27 a.u.) contains stretching contributions from C8–C10, C9–C11 and C5–N3, indicating a coupled stretching axis that links the ring framework to the N3-containing segment. The vibration at 1253.63 cm⁻¹ (I = 182.16 a.u.) is attributed to antisymmetric stretching of the C11–C10–C8 fragment coupled with ν(C5–N3), reinforcing the participation of the bridge region in the mid-frequency vibrational response and indicating coupling from the nitrogen-containing linkage into the conjugated skeleton.

3.2.4.3 C–H bending and coupled modes

Bands at 1386.95 cm⁻¹ (I = 239.48 a.u.) and 1189.27 cm⁻¹ (I = 159.73 a.u.) are dominated by in-plane δ(C–H) bending of C8–H12 and C9–H13, indicating significant participation of peripheral aromatic hydrogens in the vibrational manifold. The 1159.49 cm⁻¹ feature (I = 139.26 a.u.) corresponds to ν(N3–C7) coupled with δ(C8–H12) and δ(C9–H13), demonstrating direct coupling between the N3–C7 linkage and aromatic C–H deformations. A lower-frequency mixed vibration at 1043.61 cm⁻¹ (I = 65.83 a.u.) combines δ(C–H) bending with ν(C10–C11), reflecting secondary coupling pathways within the ring framework.

3.2.4.4 In-plane scissoring and deformation modes

Distinct deformation bands occur at 547.08 cm⁻¹ (I = 77.24 a.u.) and 892.74 cm⁻¹ (I = 47.74 a.u.). The 547.08 cm⁻¹ mode is assigned to in-plane scissoring (angle deformation) of the C4–C6–C7 and C6–C7–N3 angles, indicating deformation localized around the heteroatom-containing region. The 892.74 cm⁻¹ band corresponds to in-plane scissoring within the C11–C10–C8 and C10–C11–C9 fragments, representing coordinated deformation of the conjugated skeleton.

3.2.4.5 Overall spectral features and implications

ISTA-10B shows an exceptionally intense mixed skeletal stretching band at 1558.29 cm⁻¹, two distinct carbonyl stretching bands at 1665.87 cm⁻¹ and 1705.15 cm⁻¹ consistent with non-equivalent C=O environments, and prominent backbone modes involving C5–N3 and N3–C7 coupled with aromatic δ(C–H) deformations. The appearance of well-defined in-plane scissoring modes further indicates a mechanically coupled and relatively rigid conjugated framework. These spectral characteristics are consistent with the delocalization trends inferred from the NBO analysis and align with the conjugation effects reflected in the UV–Vi’s response [7].

Table 6 Vibrational Spectra of ISTA10B

S.NO	FREQ	SCALED FREQ	INTENSITY	DESCRIPTION
1	1621.00	1558.29	764.6106	Antisymmetric stretch of C11-C9-C5 bond and C9-C5-N3 bond coupled with stretching vibration of C4-C8 bond and bending mode of C8-H12 bond
2	1732.39	1665.87	475.9418	Stretching vibration of C7-O2 bond
3	1773.77	1705.15	312.4683	Stretching vibration of C6-O1 bond
4	1544.51	1484.73	258.5564	Antisymmetric stretch of C4-C5-C9 and C11-C10-C8
5	1442.79	1386.95	239.4839	Bending mode of C8-H12 bond and C9-H13 bond
6	1423.02	1367.95	215.2725	Stretching vibration of C8-C10, C9-C11 and C5-N3 bond
7	1304.09	1253.63	182.1616	Antisymmetric stretch of C11-C10-C8 coupled with stretching vibration of C5-N3 bond
8	1237.15	1189.27	159.7341	Bending mode of C8-H12 bond and C9-H13 bond
9	1206.17	1159.49	139.2568	Stretching vibration of N3-C7 bond coupled with bending mode of C8-H12 bond and C9-H13 bond
10	569.10	547.08	77.2404	In plane bending of C4-C6-C7 and C6-C7-N3 (Scizzoring)
11	1085.63	1043.61	65.8348	Bending mode of C8-H12 bond and C9-H13 bond coupled with stretching mode of C10-C11 bond
12	928.68	892.74	47.7432	In plane bending of C11-C10-C8 bond and C10-C11-C9 bond (Scizzoring)

3.2.5 ISTA-10C

3.2.5.1 Carbonyl and extended π-system stretching

The scaled IR spectrum of ISTA-10C (Table 7) exhibits an intense conjugation-driven skeletal stretching band in the ~1556 cm^{-1} region, accompanied by two distinct carbonyl stretching modes and several mixed ring/bridge vibrations involving the C5–N3 and N3–C7 linkages. The overall vibrational pattern indicates strong mode mixing across the conjugated framework, consistent with a resonance-stabilized anionic enol structure. The most intense feature occurs at 1556.14 cm^{-1} (I = 771.19 a.u.) and is assigned to a mixed skeletal stretching vibration comprising ν(C4–C8), ν(C9–C11) and ν(C5–N3). The dominance and high intensity of this band reflect strong coupling along the principal conjugation pathway, including the nitrogen-containing bridge segment. Two prominent carbonyl-associated bands are observed at 1665.75 cm^{-1} (I = 491.97 a.u.) and 1705.80 cm^{-1} (I = 316.17 a.u.), assigned to ν(C7=O2) and ν(C6=O1), respectively. The persistence of two ν(C=O) bands supports non-equivalent carbonyl environments under the anionic electronic distribution. In agreement with the coupled-mode character in this series, ν(C7=O2) appears more integrated with the conjugated vibrational manifold, whereas ν(C6=O1) remains comparatively more localized.

3.2.5.2 Ring and bridge-coupling vibrations

A strong mixed mode at 1384.30 cm^{-1} (I = 285.96 a.u.) is dominated by in-plane δ(C8–H12) and δ(C9–H13) bending coupled with antisymmetric stretching of the C4–C5–N3 fragment. This coupling indicates that aromatic C–H deformations are dynamically linked to the conjugated backbone through the heteroatom-containing bridge. The vibration at 1478.93 cm^{-1} (I = 280.30 a.u.) corresponds to antisymmetric skeletal stretching involving the C11–C10–C8 fragment together with stretching along the C5–C4 portion of the ring, reflecting cooperative motion across the conjugated backbone. The band at 1249.53 cm^{-1} (I = 183.99 a.u.) is a composite vibration combining antisymmetric stretching of C11–C10–C8 with ν(C5–N3), coupled with in-plane δ(C8–H12)/δ(C9–H13), reinforcing the role of the C5–N3 linkage as a key vibrational conduit within the resonance network. An additional backbone band at 1363.12 cm⁻¹ (I = 181.72 a.u.) involves stretching contributions from C8–C10, C9–C11 and C5–N3, indicating a multi-center coupling axis across the aromatic framework.

3.2.5.3 Mid-IR bending and N3–C7 coupling

Bands at 1159.64 cm⁻¹ (I = 149.68 a.u.) and 1189.17 cm⁻¹ (I = 143.78 a.u.) are dominated by aromatic in-plane δ(C–H) bending (C8–H12, C9–H13) with contributions from ν(N3–C7), indicating vibrational coupling between the N3–C7 linkage and the aromatic periphery. The feature at 1037.07 cm⁻¹ (I = 52.92 a.u.) contains in-plane scissoring within the C11–C10–C8 fragment coupled with δ(C–H) motion, reflecting coordinated deformation of the ring skeleton.

3.2.5.4 Lower-frequency in-plane scissoring modes

In the lower-frequency region, 539.29 cm⁻¹ (I = 76.24 a.u.) corresponds to a coupled in-plane scissoring deformation involving the C6–C7–N3 angle and the C11–C10–C8 fragment, consistent with deformation around the heteroatom-containing core. The 877.05 cm⁻¹ band (I = 52.95 a.u.) is assigned to in-plane scissoring of C11–C10–C8 coupled with ν(C5–N3), indicating continued coupling between the bridge linkage and the aromatic framework even within the deformation region.

3.2.5.5 Overall spectral features and implications

ISTA-10C is characterized by an exceptionally intense mixed skeletal stretching band at 1556.14 cm⁻¹ involving the principal conjugated pathway (C4–C8/C9–C11/C5–N3), two distinct ν(C=O) bands at 1665.75 cm⁻¹ and 1705.80 cm⁻¹ indicating non-equivalent carbonyl environments, and strong mixed modes linking C5–N3 and N3–C7 vibrations with aromatic δ(C–H) deformations. The presence of defined in-plane scissoring features further supports a mechanically coupled and relatively rigid conjugated framework. These vibrational trends are consistent with the delocalization patterns inferred from the NBO analysis and align with the conjugation-dependent spectral response in the TD-DFT/UV–Vis spectra [7].

Table 7 Vibrational Spectra of ISTA10C

S.NO	FREQ	SCALED FREQ	INTENSITY	DESCRIPTION
1	1618.76	1556.14	771.1869	Stretching vibration of C4-C8, C9-C11 and C5-N3 bond
2	1732.27	1665.75	491.9742	Stretching vibration of C7-O2 bond
3	1774.44	1705.80	316.1680	Stretching vibration of C6-O1 bond
4	1440.01	1384.30	285.9621	Bending mode of C8-H12 and C9-H13 coupled with antisymmetric stretch of C4-C5-N3 bond
5	1538.48	1478.93	280.2970	Antisymm stretch of C11-C10-C8 bond and C-C5-C4 bond
6	1299.82	1249.53	183.9852	Antisymm stretch of C11-C10-C8 bond along with stretching vibration of C5-N3 coupled with bending mode of C8-H12 and C9-H13 bond
7	1417.97	1363.12	181.7152	Stretching vibration of C8-C10, C9-C11 and C5-N3 bond
8	1206.33	1159.64	149.6788	Stretching vibration of N3-C7 bond coupled with bending mode of C8-H12 and C9-H13
9	1237.05	1189.17	143.7816	Bending mode of C8-H12 and C9-H13
10	561.00	539.29	76.2373	In plane bending of C6-C7-N3 (Scizzoring) and C11-C10-C8
11	912.36	877.05	52.9519	In plane bending of C11-C10-C8 (Scizorring) coupled with stretching vibration of C5-N3
12	1078.80	1037.07	52.9177	In plane bending of C11-C10-C8 (Scizorring) coupled with bending mode of C8-H12 and C9-H13

3.2.6 ISTA-10D

3.2.6.1 Major stretching vibrations and conjugation indicators

The scaled IR spectrum of ISTA-10D (fluoro-substituted isatin anion) in Table 8 shows intense conjugation-driven skeletal stretching in the ~1560–1705 cm⁻¹ region together with prominent mixed modes involving the C5–N3/N3–C7 linkages and aromatic C–H deformations. In addition, a characteristic C–F stretching contribution appears in the ~1170 cm⁻¹ region, indicating participation of the fluoro-substitution site in the vibrational response of the conjugated framework. A strong mixed skeletal stretching band occurs at 1560.02 cm⁻¹ (I = 522.90 a.u.) and is assigned to ν(C4–C8), ν(C9–C11) and ν(C5–N3). The intensity and mixed character of this band indicate efficient coupling along the principal conjugated pathway, including the nitrogen-bridged segment. Two distinct carbonyl bands are observed at 1666.07 cm⁻¹ (I = 497.03 a.u.) and 1704.86 cm⁻¹ (I = 295.58 a.u.). The 1666.07 cm⁻¹ vibration corresponds predominantly to ν(C7=O2), with additional contribution from antisymmetric stretching associated with the adjacent framework (as indicated by the normal-mode decomposition), suggesting that the C7=O2 site is more integrated with the conjugated manifold than the second carbonyl. The 1704.86 cm⁻¹ band is assigned to ν(C6=O1) and appears comparatively more localized, consistent with weaker coupling to the conjugated framework relative to ν(C7=O2).

3.2.6.2 Bending and mixed ring-coupled vibrations

A prominent mixed mode at 1211.87 cm⁻¹ (I = 277.72 a.u.) involves antisymmetric stretching of the C6–C7–N3 linkage coupled with in-plane scissoring within the C9–C5–N3 fragment and in-plane δ(C–H) bending (C8–H12 and C11–H13). This band highlights strong coupling between the bridge region and the aromatic periphery, consistent with a dynamically connected resonance framework. The vibration at 1427.43 cm⁻¹ (I = 252.95 a.u.) corresponds to a symmetric framework mode centered on the C10–C8–C4 fragment, coupled with ν(C9–C11) and ν(C5–N3), indicating multi-center coupling across the aromatic skeleton. The 1356.59 cm⁻¹ band (I = 231.14 a.u.) contains ν(C5–N3) and ν(C9–C11) contributions coupled with δ(C8–H12), further supporting strong interaction between the nitrogen-linked bridge and ring motion.

3.2.6.3 Antisymmetric backbone coupling across the core framework

The mid-frequency region contains several antisymmetric backbone modes that reflect extensive coupling within the conjugated skeleton. The band at 1263.95 cm⁻¹ (I = 170.99 a.u.) is assigned to an antisymmetric skeletal stretch involving the C11–C10–C8, C10–C8–C4, C8–C4–C5, C4–C5–C9 and C9–C5–N3 fragments, indicating delocalized vibrational participation across the ring and bridge. At 1247.56 cm⁻¹ (I = 138.97 a.u.), antisymmetric stretching of N3–C5–C4 is coupled with ν(C8–C10) and in-plane scissoring of the C9–C11–H13 fragment, showing that peripheral δ(C–H) deformation remains coupled to the backbone stretching manifold. The 1509.06 cm⁻¹ mode (I = 114.08 a.u.) includes antisymmetric stretching contributions from C11–C10–C8 and C9–C5–C4 coupled with scissoring components (C10–C8–C4 and H13–C11–C9), reflecting coordinated deformation across the conjugated skeleton.

3.2.6.4 Fluoro group and terminal stretching motions

A diagnostic feature at 1176.59 cm⁻¹ (I = 96.61 a.u.) is assigned to ν(C9–F15) coupled with δ(C–H) bending (C8–H12 and C11–H13). The coupling of ν(C–F) with aromatic deformations indicates that substitution at the fluorinated site is mechanically integrated into the ring vibrational response. The band at 1108.00 cm⁻¹ (I = 77.37 a.u.) corresponds to ν(N3–C7) coupled with δ(C–H) bending, reinforcing the recurring role of the N3–C7 linkage as a key vibrational contributor across the substituted series.

3.2.6.5 Overall spectral features and implications

ISTA-10D is characterized by an intense conjugation-driven skeletal stretching band at 1560.02 cm⁻¹ involving ν(C4–C8)/ν(C9–C11)/ν(C5–N3), two distinct carbonyl stretching bands at 1666.07 cm⁻¹ and 1704.86 cm⁻¹ consistent with non-equivalent C=O environments, multiple mixed backbone modes that couple the C5–N3/N3–C7 bridge with aromatic δ(C–H) deformations, and a diagnostic ν(C9–F) feature at 1176.59 cm⁻¹ coupled to ring motions. Collectively, these features are consistent with a strongly coupled and resonance-stabilized anionic framework and indicate substitution-dependent redistribution of coupling and intensity, in agreement with the electronic delocalization trends in the NBO and UV–Visible spectra [7].

Table 8 Vibrational Spectra of ISTA10D

S.NO	FREQ	SCALED FREQ	INTENSITY	DESCRIPTION
1	1622.80	1560.02	522.9007	Stretching vibration of C4-C8, C9-C11 and C5-N3 bonds
2	1732.60	1666.07	497.0323	Antisymmetric Stretching vibration of C5-C9-C3 bond coupled with stretching vibration of C7-O2 bond
3	1773.47	1704.86	295.5811	Stretching vibration C6-O1 bond
4	1260.64	1211.87	277.72267	Antisymmetric stretching of C6-C7-N3 bond along with in plane bending of C9-C5-N3 bond (scizzoring) and in plane bending of C8-H12 bond and C11-H13 bond
5	1484.91	1427.43	252.9482	Symmetric mode of vibration of C10-C8-C4 coupled with stretching mode of vibration of C9-C11 bond and C5-N3 bond
6	1411.21	1356.59	231.1438	Stretching mode of vibration of C5-N3 bond, C9-C11 bond coupled with bending mode of C8-H12 bond
7	1314.83	1263.95	170.9876	Antisymmetric sstretch of C11-C10-C8, C10-C8-C4, C8-C4-C5, C4-C5-C9 and C9-C5-N3
8	1297.78	1247.56	138.9661	Antisymmetric stretch of N3-C5-C4 along with stretching vibration of C8-C10 coupled with in plane bending of C9-C11-H13 (scizzoring)
9	1569.83	1509.06	114.0823	Antisymmetric stretch of C11-C10-C8, C9-C5-C4 coupled with in plane bending of C10-C8-C4 (scizzoring) and H13-C11-C9 (scizzoring)
10	1223.93	1176.59	96.6127	Stretching vibration of C9-F15 coupled with bending mode of C8-H12 and C11-H13
11	1152.59	1108.00	77.3688	Stretching mode of N3-C7 coupled with bending mode of C8-H11 and C11-H13

3.2.7 ISTA-10E

3.2.7.1 Carbonyl and backbone stretching vibrations

The scaled IR spectrum of ISTA-10E in Table 9 is characterized by two strong carbonyl stretching bands together with an intense conjugation-driven skeletal mode in the ~1553 cm⁻¹ region. Several mid-frequency vibrations show extensive mixing between backbone stretching and in-plane scissoring/rocking motions, consistent with a mechanically coupled and resonance-stabilized anionic framework. In addition, a diagnostic C–Cl stretching contribution appears in the ~782 cm⁻¹ region, indicating vibrational participation of the halogen-substituted site. A high-intensity band at 1668.25 cm⁻¹ (I = 547.48 a.u.) is assigned primarily to ν(C7=O2) coupled with ν(C9–C5), indicating vibrational communication between the carbonyl site and the conjugated aromatic core. The second carbonyl stretch appears at 1706.71 cm⁻¹ (I = 299.52 a.u.) and is assigned to ν(C6=O1), remaining comparatively more localized than the ν(C7=O2) vibration. The strong band at 1552.92 cm⁻¹ (I = 504.62 a.u.) corresponds to a mixed skeletal stretching mode involving ν(C8–C4), ν(C11–C9) and ν(C5–N3), coupled with in-plane δ(C–H) bending of C8–H12 and C11–H13. The combined stretching–bending character supports strong coupling across the conjugated framework and highlights the dynamical involvement of the nitrogen-bridged segment.

3.2.7.2 Coupled ring vibrations and scissoring motions

A prominent mode at 1406.85 cm⁻¹ (I = 294.87 a.u.) contains stretching contributions from C10–C8, C11–C9 and C5–N3, coupled with in-plane scissoring of H13–C11–C9 and H12–C8–C4. The mixed nature of this vibration indicates that backbone stretching is tightly linked to aromatic deformation coordinates. The band at 1343.14 cm⁻¹ (I = 245.80 a.u.) combines ν(C11–C9) with antisymmetric stretching of the C4–C5–N3 fragment, again coupled with scissoring of H12–C8–C4. This assignment emphasizes the central role of the C4–C5–N3 linkage as a conduit for vibrational coupling across the ring system. At 1264.07 cm⁻¹ (I = 201.36 a.u.), stretching of C10–C11 and C5–N3 is coupled with scissoring motions involving H13–C11–C9 and H12–C8–C4, reinforcing the repeated participation of the nitrogen-linked bridge and adjacent aromatic segments in the mid-frequency vibrational response.

3.2.7.3 Mid-frequency backbone and mixed coupling modes

Bands at 1131.44 cm⁻¹ (I = 136.48 a.u.) and 1211.55 cm⁻¹ (I = 130.44 a.u.) are assigned to ν(N3–C7) coupled with stretching in the C11–C9 region and in-plane δ(C–H) bending (C11–H13, C8–H12). These features indicate coupling between the N3–C7 linkage and aromatic deformations. The 1486.84 cm⁻¹ mode (I = 115.12 a.u.) corresponds to antisymmetric stretching of C11–C10–C8 and C9–C5–C4 coupled with scissoring of H13–C11–C9 and H12–C8–C4, reflecting coordinated deformation across both sides of the conjugated skeleton. A lower-intensity composite antisymmetric stretching vibration at 1241.30 cm⁻¹ (I = 76.07 a.u.) includes contributions from C11–C10–C8, C9–C11–C10, C9–C5–C4 and N3–C5–C4, indicating ring-wide coupling within the backbone.

3.2.7.4 Halogen-related and lower-frequency vibrations

A diagnostic band at 781.82 cm⁻¹ (I = 62.53 a.u.) is assigned to ν(C9–Cl15) coupled with ν(C6–C7) and in-plane deformation components (including scissoring/rocking contributions). This feature provides a useful marker for halogen substitution in this derivative. The 1082.17 cm⁻¹ band (I = 51.24 a.u.) corresponds to a mixed skeletal vibration involving C4–C6, N3–C7, C9–C5, C4–C5 and C9–Cl15 stretching contributions coupled with in-plane scissoring (C10–C8–C4 and C4–C5–C9), reflecting substitution-sensitive coupling in the lower mid-frequency region.

3.2.7.5 Overall spectral features and implications

ISTA-10E exhibits an intense ν(C7=O2) band at 1668.25 cm⁻¹ coupled with the conjugated ring, a distinct ν(C6=O1) band at 1706.71 cm⁻¹ that is comparatively localized, a strong mixed skeletal stretching mode at 1552.92 cm⁻¹ involving ν(C8–C4)/ν(C11–C9)/ν(C5–N3) with δ(C–H) coupling, and multiple mid-frequency modes dominated by combined backbone stretching and in-plane scissoring coordinates. The presence of a clear ν(C–Cl) contribution near 781.82 cm⁻¹ further confirms substituent participation in the vibrational response. Collectively, these features are consistent with a strongly coupled, resonance-stabilized anionic framework and align with the electronic delocalization trends in the NBO and UV–Visible analysis [7].

Table 9 Vibrational Spectra of ISTA10E

S.NO	FREQ	SCALED FREQ	INTENSITY	DESCRIPTION
1	1734.37	1668.25	547.4849	Stretching vibration of C9-C5 and C7-O2
2	1615.41	1552.92	504.6195	Stretching vibration of C8-C4, C11-C9, and C5-N3 bond coupled with bending mode of C8-H12 and C11-H13
3	1775.39	1706.71	299.5170	Stretching vibration of C6-O1
4	1463.47	1406.85	294.8701	Stretching vibration of C10-C8, C11-C9 and C5-N3 bond coupled with bending mode of H13-C11 and H12-C8-C4 (Scizzoring)
5	1397.23	1343.14	245.7986	Stretching vibration of C11-C9 bond and antisymmetric stretch of C4-C5-N3 coupled with bending mode of H12-C8-C4 (Scizzoring)
6	1314.95	1264.07	201.3620	Stretching vibration of C10-C11, C5-N3 coupled with bending mode of H13-C11-C9 (Scizzoring) and H12-C8-C4 (Scizzoring)
7	1176.97	1131.44	136.4792	Stretching vibration of N3-C7 and C11-C9 coupled with bending mode of C11-H13 and C8-H12

8	1260.31	1211.55	130.4412	Stretching vibration of N3-C7 coupled with bending mode of H13-C11 and H12-C8
9	1546.65	1486.84	115.1243	Antisymmetric vibration of C11-C10-C8 and C9-C5-C4 coupled with in plane bending mode of vibration of H13-C11-C9 (Scizzoring) and H12-C8-C4 (Scizzoring)
10	1291.25	1241.30	76.0673	Antisymmetric stretch of C11-C10-C8, C9-C11-C10, C9-C5-C4, N3-C5-C4 and
11	813.29	781.82	62.5308	Stretching of C9-Cl15 bond and C6-C7 bond coupled with in plane bending of C10-C8-C4 (Scizzoring) and H13-C11-C9 (Rocking)
12	1125.70	1082.17	51.2396	Stretching of C4-C6, N3-C7, C9-C5, C4-C5 and C9-Cl15 bond coupled with in plane bending of C10-C8-C4 (Scizzoring) and C4-C5-C9 (Scizzoring)

3.2.8 ISTA-10F

3.2.8.1 Carbonyl and backbone stretching vibrations

The scaled IR spectrum of ISTA-10F displays high-intensity carbonyl stretching bands along with a strong conjugation-driven skeletal mode near 1552 cm^{-1}. The mid-frequency region is dominated by mixed backbone stretching coupled with pronounced in-plane scissoring/rocking motions of aromatic C–H groups, indicating extensive vibrational coupling across the substituted π-framework. Overall, the spectral pattern is consistent with a strongly coupled and resonance-stabilized anionic system. A high-intensity band at 1667.57 cm^{-1} (I = 563.11 a.u.) is assigned primarily to ν(C7=O2) coupled with antisymmetric stretching within the C9–C5–N3 fragment. The coupling of the carbonyl stretch with the N3-linked ring segment indicates vibrational communication between the carbonyl site and the conjugated framework. The second carbonyl stretch occurs at 1707.47 cm^{-1} (I = 306.26 a.u.) and is assigned to ν(C6=O1), remaining comparatively more localized relative to the ν(C7=O2) band. The intense mixed skeletal band at 1551.50 cm^{-1} (I = 510.90 a.u.) comprises stretching contributions from ν(C4–C8), ν(C9–C11) and ν(C5–N3), with contributions from the O2–C7 moiety, reflecting cooperative motion along the main conjugation pathway of the anionic framework.

3.2.8.2 Ring-coupled stretching and C–H scissoring modes

A prominent mixed mode at 1402.42 cm^{-1} (I = 304.81 a.u.) involves stretching contributions from C9–C11, C8–C10 and C5–N3, coupled with in-plane scissoring deformations (H13–C11–C10 and C4–C8–H12). This assignment highlights coupling between backbone stretching coordinates and peripheral C–H deformation modes. The band at 1340.08 cm^{-1} (I = 250.29 a.u.) is assigned to antisymmetric stretching within N3–C5–C4 and C5–C9–C11, coupled with scissoring of H12–C8–C10, indicating coordinated deformation across the substituted ring framework. At 1263.04 cm^{-1} (I = 186.66 a.u.), stretching of C5–N3 and C10–C11 is coupled with in-plane scissoring of H12–C8–C4 and H13–C11–C9, demonstrating that bridge and terminal ring segments participate within the same coupled vibrational manifold.

3.2.8.3 Bridge-linkage vibrations and mixed backbone deformation

The 1128.55 cm^{-1} band (I = 138.35 a.u.) corresponds to ν(N3–C7) coupled with δ(C8–H12) and rocking deformation of the H13–C11–C9 fragment, indicating coupling between the N3–C7 linkage and the aromatic periphery. A related vibration at 1211.52 cm^{-1} (I = 112.23 a.u.) is also assigned to ν(N3–C7) coupled with bending of H13–C11 and H12–C8, reinforcing the recurring role of the N3–C7 linkage as a key coupling coordinate in these derivatives. A mixed antisymmetric skeletal mode at 1479.28 cm^{-1} (I = 108.95 a.u.) involves stretching of the C11–C10–C8 and C9–C5–C4 fragments coupled with scissoring of H13–C11–C9 and H12–C8–C4, reflecting coordinated deformation across both sides of the conjugated backbone.

3.2.8.4 Lower-frequency scissoring and ring deformation modes

A composite band at 1238.44 cm^{-1} (I = 91.86 a.u.) contains antisymmetric stretching contributions from C11–C10–C8, C9–C11–C10, C5–C9–C11 and C4–C5–C9 together with symmetric stretching of C9–C5–N3, coupled with H13–C11 bending. This mode indicates ring-wide coupling within the backbone. Lower-frequency deformation features include 754.41 cm⁻¹ (I = 51.95 a.u.), assigned to combined scissoring of C5–C9–C11 and C4–C8–C10 with rocking of C9–C11–H13 and contribution from ν(C6–C7), and 1073.78 cm⁻¹ (I = 44.87 a.u.), assigned to antisymmetric stretching across multiple backbone linkages (C4–C5–C9, C5–C9–C11, C9–C11–C10, C11–C10–C8) coupled with symmetric stretching of N3–C5–C9 and C–H bending.

3.2.8.5 Overall spectral features and implications

ISTA-10F is characterized by (i) an intense ν(C7=O2) band at 1667.57 cm⁻¹ coupled with the C9–C5–N3 fragment, (ii) a distinct ν(C6=O1) band at 1707.47 cm⁻¹ that remains comparatively localized, and (iii) a strong mixed skeletal mode at 1551.50 cm⁻¹ involving ν(C4–C8)/ν(C9–C11)/ν(C5–N3) with contribution from the O2–C7 moiety. The mid-IR region shows extensive coupling between backbone stretching and in-plane scissoring/rocking deformations of aromatic C–H groups, while lower-frequency deformation modes provide additional markers of coordinated ring motion in the substituted framework. Collectively, these features are consistent with a strongly coupled, resonance-stabilized anionic structure and align with the substitution-dependent electronic delocalization trends in the NBO and UV–Vis spectroscopy [7].

Table 10 Vibrational Spectra of ISTA10F

S.NO	FREQ	SCALED FREQ	INTENSITY	DESCRIPTION
1	1734.70	1668.57	563.1131	Stretching vibration of C7-O2 coupled with antisymmetric stretch of C9-C5-N3
2	1613.96	1551.52	510.9031	Stretching vibration of C4-C8, C9-C11, C5-N3 and C7-O2 bonds
3	1776.21	1707.50	306.2586	Stretching vibration of C6-O1 bond
4	1458.88	1402.43	304.8147	Stretching vibration of C9-C11, C8-C10 and C5-N3 bond coupled with in plane bending of H13-C11-C10 (Scizzoring) and C4-C8-H12 (Scizzoring)
5	1394.03	1340.06	250.2903	Antisymmetric stretch of N3-C5-C4 and C5-C9-C11 coupled with bending mode of H12-C8-C10 (Scizzoring)
6	1313.89	1263.05	186.6629	Stretching vibration of C5-N3 and C10-C11 coupled with bending mode of vibration of H12-C8-C4 (Scizzoring) and H13-C11-C9 (Scizzoring)
7	1173.98	1128.57	138.3508	Stretching vibration of C7-N3 coupled with bending mode of H12-C8 bond coupled with H13-C11-C9 (rocking)
8	1260.29	1211.53	112.2268	Stretching vibration of N3-C7 bond coupled with bending mode of H13-C11 and H12-C8 bond
9	1538.83	1479.29	108.9528	Antisymmetric stretch of C11-C10-C8 and C9-C5-C4 coupled with bending mode of H13-C11-C9 (Scizzoring) and H12-C8-C4 (Scizzoring)
10	1288.30	1238.44	91.8570	Antisymmetric stretch of C11-C10-C8, C9-C11-C10, C5-C9-C11, C4-C5-C9 and symmetric stretch of C9-C5-N3 coupled with bending mode of H13-C11
11	784.78	754.42	51.9460	Bending mode of C5-C9-C11 (Scizzoring), C4-C8-C10 (Scizzoring) and C9-C11-H13 (Rocking) and stretching mode of C6-C7
12	1117.01	1073.81	44.8729	Antisymmetric stretch of C4-C5-C9, C5-C9-C11, C9-C11-C10, C11-C10-C8 and symmetric stretch of N3-C5-C9 coupled with bending mode of C11-H13

3.3 Integrated correlation of NBO, UV–Vis, IR, and NMR results

Across the halogen-substituted anionic enol series, the IR, NMR, TD-DFT/UV–Vis, and NBO results are mutually consistent and collectively indicate substitution-dependent redistribution of electron density within a strongly conjugated framework. The scaled IR spectra of all derivatives are dominated by an intense conjugation-driven mixed skeletal vibration in the ~1550–1570 cm^{-1} region, accompanied by two clearly separated carbonyl stretching bands assigned to ν(C7=O2) and ν(C6=O1), typically appearing in the ~1660–1707 cm^{-1} region. The persistence of two distinct ν(C=O) features supports non-equivalent carbonyl environments and is consistent with vibrational coupling between the aromatic backbone and the heteroatom-containing enolate/lactam segment. The NMR data reflect the same electronic asymmetry and resonance redistribution. The carbonyl carbon C6 remains the most deshielded site across the series (typically ~208–210 ppm), with C7 also consistently downfield (~180–182 ppm), consistent with strongly polarized C=O centers. In contrast, ring positions along the principal delocalization pathways show the greatest substitution sensitivity, with pronounced chemical-shift changes at sites where charge redistribution is largest—most notably C9 in ISTA-10D ($\delta \approx 160.92$ ppm; $q > 0$) and C11 in ISTA-10A ($\delta \approx 177.47$ ppm; $q > 0$)—supporting the view that substituent-driven electron withdrawal/redistribution produces measurable deshielding at the electronically perturbed positions. This spectroscopic behavior is rationalized at the orbital level by the NBO analysis [7]. Lone-pair donation from N3 into adjacent π* acceptor orbitals associated with the carbonyl/enolate unit and the aromatic π-network (e.g., $n(N3) \rightarrow \pi^*(O2–C7)$ and $n(N3) \rightarrow \pi^*(C4–C5)$) identifies N3 as a key resonance hub, while additional $\pi \rightarrow \pi^*$ delocalization across the ring stabilizes the anionic scaffold. These donor–acceptor pathways provide a ground-state electronic basis for the intense, mixed skeletal IR mode (large dipole-moment change distributed over the conjugated backbone) and the persistent carbonyl asymmetry manifested as two ν(C=O) bands. The convergence of IR mode mixing with carbonyl non-equivalence, charge-sensitive NMR deshielding at electronically responsive ring sites, TD-DFT visible-region red shifts, and NBO-quantified delocalization pathways provides a coherent multi-spectroscopic validation that halogen substitution systematically tunes resonance pathways and electron delocalization in the anionic enol forms of isatin [7].

IV. CONCLUSION

This work provides a unified theoretical description of the anions of the enol (lactim) form of isatin and its halogen-substituted derivatives, with emphasis on how halogen substitution modulates spectroscopic signatures through resonance-driven redistribution of electron density. A key contribution of the study is the internally consistent linkage established between ground-state electronic structure (NBO descriptors) and two independent spectroscopic outcomes (IR and NMR) for anionic lactim systems, which remain considerably less explored than the corresponding neutral isatin derivatives. At the B3LYP/6-311++G(d,p) level, the vibrational analysis yields a clear and reproducible spectral pattern across the entire series: a dominant conjugation-controlled mixed skeletal vibration in the mid-IR region, accompanied by two well-resolved carbonyl stretching modes assignable to C7=O2 and C6=O1. The persistence of two ν(C=O) bands across all derivatives supports sustained carbonyl non-equivalence and indicates systematic coupling between the aromatic scaffold and the heteroatom-containing enolate/lactim segment in the anionic framework. Complementary GIAO H-1 and C-13 NMR calculations in DMSO further corroborate this electronic asymmetry, with the carbonyl carbons remaining consistently deshielded and with pronounced substitution-sensitive responses at selected ring positions, thereby identifying the sites most strongly affected by halogen-driven charge redistribution. A central outcome is the quantitative charge–shift relationship observed across the eight species. Regression analysis reveals very strong correlations between computed C-13 chemical shifts and NBO natural charges, supporting a rigorous and general conclusion that local shielding trends are governed primarily by electronic reorganization within the conjugated π-system. The donor–acceptor interactions *viz.* $n \rightarrow \pi^*$ and $\pi \rightarrow \pi^*$ delocalization framework that rationalizes the NMR deshielding trends also provides a mechanistic basis for the enhanced IR intensities and mixed vibrational character of the key skeletal modes, yielding a coherent explanation that is consistent across spectroscopic probes. Overall, this study establishes a correlation-based spectroscopic framework linking NBO delocalization with IR mode mixing/intensity and NMR shielding behavior in anionic isatin lactim systems, and demonstrates that halogen substitution can serve as a predictable handle for tuning resonance stabilization and measurable spectroscopic response. Beyond providing reliable reference assignments for IR and NMR across the derivative set, the results offer a mechanistically grounded strategy for designing isatin-derived anionic frameworks with tailored electronic structure and diagnostically responsive spectral fingerprints.

ACKNOWLEDGEMENT

Authors are thankful to Shyama Prasad Vidyalaya Lodi Estate and Amit Kumar, Department of Chemistry, University of Delhi for supporting this work

REFERENCES

[1] Varun; Sonam, S.; Kakkar, R. Isatin and its derivatives: a survey of recent syntheses, reactions, and applications. *MedChemComm* 2019.

[2] Naumov, P.; Anastasova, F. Experimental and theoretical vibrational study of isatin, its 5-(NO2, F, Cl, Br, I, CH3) analogues and the isatinato anion. *Spectrochimica Acta Part A* 2001, 57, 469–481. https://doi.org/10.1016/S1386-1425(00)00393-0

[3] Tisovský, P.; et al. Effect of Structure on Charge Distribution in the Isatin Anions in Aprotic Environment: Spectral Study. *Molecules* 2017, 22, 1961. https://doi.org/10.3390/molecules22111961

[4] Silverstein, R. M.; Webster, F. X.; Kiemle, D. J. Spectrometric Identification of Organic Compounds, 7th ed.; Wiley: Hoboken, 2006.

[5] Arora, E. Theoretical Study of Isatin and its Halogenated Derivatives. *Journal of Emerging Technologies and Innovative Research (JETIR)* 2024, 11(3), Paper ID JETIR2403719.

[6] Arora, E.; Gulia, S. Thermodynamic and Reactivity Parameters of Anions of Enol form of Isatin and its Halogenated Derivatives: A Theoretical Study. *International Journal of Innovative Research in Technology (IJIRT)* 2025, 12(7), 4387–4397 (Paper ID 189025).

[7] Arora, E.; Gulia, S. NBO analysis and UV-Visible analysis of Anions of Enol form of Isatin and its Halogenated Derivatives: A Theoretical Study. *International Journal of Innovative Research in Technology (IJIRT)* 2026, 12(9), 1785–1796 (Paper ID 192582).

[8] Lee, C.; Yang, W.; Parr, R. G. Development of the Colle–Salvetti correlation-energy formula into a functional of the electron density. *Phys. Rev. B* 1988, 37, 785–789. https://doi.org/10.1103/PhysRevB.37.785

[9] Stephens, P. J.; Devlin, F. J.; Chabalowski, C. F.; Frisch, M. J. Ab initio calculation of vibrational absorption and circular dichroism spectra using density functional force fields. *J. Phys. Chem.* 1994, 98, 11623–11627. https://doi.org/10.1021/j100096a001

[10] Merrick, J. P.; Moran, D.; Radom, L. An evaluation of harmonic vibrational frequency scale factors. *J. Phys. Chem. A* 2007, 111, 11683–11700. https://doi.org/10.1021/jp073974n

[11] Wolinski, K.; Hinton, J. F.; Pulay, P. Efficient implementation of the gauge-independent atomic orbital (GIAO) method for NMR chemical shift calculations. *J. Am. Chem. Soc.* 1990, 112, 8251–8260. https://doi.org/10.1021/ja00179a005

[12] Tomasi, J.; Mennucci, B.; Cammi, R. Quantum mechanical continuum solvation models. *Chem. Rev.* 2005, 105, 2999–3093. https://doi.org/10.1021/cr9904009

[13] Frisch, M. J.; Trucks, G. W.; Schlegel, H. B.; et al. Gaussian 09, Gaussian, Inc., Wallingford CT, 2009 (cite the specific revision used).

[14] Velcheva, E. A.; Vassileva-Boyadjieva, P. J.; Binev, I. G. Experimental and DFT studies on IR spectral and structural changes arising from the conversion of 1H-indole-2,3-dione (isatin) into azanion. *Bulgarian Chemical Communications* 2008, 40(4), 433–439.

[15] Glendening, E. D.; Landis, C. R.; Weinhold, F. NBO 6.0: Natural bond orbital analysis program. *J. Comput. Chem.* 2013. https://doi.org/10.1002/jcc.23266

[16] Weinhold, F.; Landis, C. R. Valency and Bonding: A Natural Bond Orbital Donor–Acceptor Perspective; Cambridge University Press, 2005.

[17] Kohli, E.; Arora, R.; Kakkar, R. Theoretical Study of the Stability of Tautomers and Conformers of Isatin-3-Thiosemicarbazone (IBT). *Canadian Chemical Transactions* 2014, 2(3), 327–342. https://doi.org/10.13179/canchemtrans.2014.02.03.0112

[18] Hammett, L. P. Physical Organic Chemistry, 2nd ed.; McGraw-Hill: New York, 1970

[19] Frisch, M. J.; Trucks, G. W.; Schlegel, H. B.; et al. Gaussian 09, Revision D.01; Gaussian, Inc.: Wallingford, CT, 2009.

[20] Becke, A. D. Density-functional thermochemistry. III. The role of exact exchange. *J. Chem. Phys.* 1993, *98*, 5648–5652. https://doi.org/10.1063/1.464913

[21] Lee, C.; Yang, W.; Parr, R. G. Development of the Colle–Salvetti correlation-energy formula into a functional of the electron density. *Phys. Rev. B* 1988, *37*, 785–789. https://doi.org/10.1103/PhysRevB.37.785

[22] Krishnan, R.; Binkley, J. S.; Seeger, R.; Pople, J. A. Self-consistent molecular orbital methods. XX. A basis set for correlated wave functions. *J. Chem. Phys.* 1980, *72*, 650–654. https://doi.org/10.1063/1.438955

[23] Frisch, M. J.; Pople, J. A.; Binkley, J. S. Effects of basis set extensions to the 6-311G basis set on reaction energies and geometries. ** *J. Chem. Phys.* 1984, *80*, 3265–3269. https://doi.org/10.1063/1.447079

[24] Merrick, J. P.; Moran, D.; Radom, L. An evaluation of harmonic vibrational frequency scale factors. *J. Phys. Chem. A* 2007, *111*, 11683–11700. https://doi.org/10.1021/jp073974n

[25] NIST Computational Chemistry Comparison and Benchmark Database (CCCBDB). Vibrational frequency scaling factors. https://cccbdb.nist.gov/vsfx.asp

[26] Wolinski, K.; Hinton, J. F.; Pulay, P. Efficient implementation of the gauge-independent atomic orbital (GIAO) method for NMR chemical shift calculations. *J. Am. Chem. Soc.* 1990, *112*, 8251–8260. https://doi.org/10.1021/ja00179a005

[27] Hoffman, R. E. Standardization of chemical shifts of TMS and solvent signals in NMR solvents. *Magn. Reson. Chem.* 2006, *44*, 606–616. https://doi.org/10.1002/mrc.1801

[28] Cossi, M.; Rega, N.; Scalmani, G.; Barone, V. *Energies, structures, and electronic properties of molecules in solution with the C-PCM solvation model.* J. Comput. Chem. 2003, *24*, 669–681. https://doi.org/10.1002/jcc.10189

[29] Tomasi, J.; Mennucci, B.; Cammi, R. *Quantum mechanical continuum solvation models.* Chem. Rev. 2005, *105*, 2999–3093. https://doi.org/10.1021/cr9904009

[30] Marenich, A. V.; Cramer, C. J.; Truhlar, D. G. *Universal solvation model based on solute electron density and a continuum model of the solvent (SMD).* J. Phys. Chem. B 2009, *113*, 6378–6396. https://doi.org/10.1021/jp810292n

[31] Wolinski, K.; Hinton, J. F.; Pulay, P. *Efficient implementation of the gauge-independent atomic orbital (GIAO) method for NMR chemical shift calculations.* J. Am. Chem. Soc. 1990, *112*, 8251–8260. https://doi.org/10.1021/ja00179a005

[32] Reed, A. E.; Weinstock, R. B.; Weinhold, F. *Natural population analysis.* J. Chem. Phys. 1985, *83*, 735–746. https://doi.org/10.1063/1.449486

[33] Glendening, E. D.; Landis, C. R.; Weinhold, F. *NBO 6.0: Natural bond orbital analysis program.* J. Comput. Chem. 2013. https://doi.org/10.1002/jcc.23266